Available online at www.sciencedirect.com
SciVerse ScienceDirect
Scripta Materialia 66 (2012) 634–637
Scripta MATERIALIA
www.elsevier.com/locate/scriptamat

Tensile deformation characteristics of bulk ultrafine-grained austenitic stainless steel produced by thermal cycling

B. Ravi Kumar[a,*] and Dierk Raabe[b]

[a] *MST Division, CSIR-National Metallurgical Laboratory, Jamshedpur, India*
[b] *Max-Planck-Institut für Eisenforschung, Max-Planck Str. 1, 40237 Düsseldorf, Germany*

Received 28 November 2011; revised 25 January 2012; accepted 25 January 2012
Available online 30 January 2012

Deformation microstructures of bulk ultrafine-grained austenitic AISI 304L stainless steels were analyzed by electron backscatter diffraction. Samples with grain sizes below 500 nm showed transition from grain-scale deformation to the collective phenomenon of shear banding. This was assisted by strain-induced grain rotation and coalescence. This phenomenon was suppressed in samples with a bimodal grain size distribution (maxima at ~650 and ~1400 nm) due to deformation-induced martensite formation, yielding high tensile strength and ductility (1348 MPa ultimate tensile strength at 0.36 max. true strain).

Keywords: Stainless steel; Ultrafine grain; Plastic deformation; Electron backscatter diffraction; Deformation-induced martensite

Bulk ultrafine-grained (UFG) materials exhibit excellent tensile strength but low tensile ductility. The increase in yield strength (YS) is due to the Hall–Petch effect [1,2]. UFG metals show an improvement in total elongation of up to 10% compared to equivalent nanostructured materials [3]. In contrast, the uniform tensile deformation is much smaller for most nanocrystalline (nc) and UFG alloys when compared to samples with larger grain size [4]. The inherent loss of ductility and toughness of many nc materials may be attributed to the very large grain boundary area that facilitates crack propagation [5]. Another reason may be the localization of plastic deformation, as was shown for nc Cu [6,7]. Similar phenomena were reported for nc Fe, in which the formation of narrow shear bands (SB) indicated strain localization [8]. Also, nc grains fail to store dislocations such as normally observed in coarse-grained metals, which hence have a higher strain-hardening capability. Studies on most nc/UFG metals showed a very flat course of their true stress–strain curves, with very limited strain hardening [9]. Various strategies have been suggested to overcome these obstacles with the aim to jointly improve ductility and strength [10,11].

Here we study the room temperature tensile deformation behavior of UFG austenitic AISI 304L (18.6% Cr, 10.1% Ni, 0.02% C; wt.%) stainless steel produced through a thermal cycling process. This process involves an initial heavy cold rolling and subsequent repeated short annealing cycles. During the thermal cycling, it was observed that, after each thermal cycle, the strain heterogeneity of the cold-deformed microstructure increased due to the evolution of some newly recrystallized strain-free austenite grains. Further, some volume fraction of subgrains was ready to assume a critical nucleus size to nucleate as strain-free grains. In addition to the above two grain types, some residual deformed regions were also retained in the microstructure. This microstructural inhomogeneity creates a non-homogeneous distribution of the stored deformation energy, which results in a spatially varying driving force of recrystallization of the microstructure. Owing to the difference in the driving forces, the recrystallization in the residual deformed region continues while growth of the freshly nucleated austenite grains is prevented.

We observed that, by the appropriate selection of temperature for the thermal cycling sequence, the grain size distribution could be varied. A more detailed description of the thermal cycling process is given elsewhere [12]. In this study, a 90% cold-rolled plate of 1 mm thickness was subjected to four thermal cycles at different temperatures so as to vary the grain size and distribution. The first two cycles consisted of isothermal annealing of the samples for 45 s at 900–950 °C followed by air cooling. The next two cycles were performed at

* Corresponding author. Fax: +91 6572345213; e-mail: ravik@nmlindia.org

1359-6462/$ - see front matter © 2012 Acta Materialia Inc. Published by Elsevier Ltd. All rights reserved.
doi:10.1016/j.scriptamat.2012.01.052

825–850 °C for 45 s. In all cases, the samples were mounted in the furnace after the desired temperature was reached to achieve rapid heating. Tensile tests were conducted at room temperature, under displacement control, at an initial strain rate of $1.3 \times 10^{-4}\ s^{-1}$ using an Instron 8862 system of 100 kN capacity. The elongation was measured by an extensometer of 25 mm gauge length. Electron backscatter diffraction (EBSD) was performed in a JEOL 6500F field emission gun scanning electron microscope and an EDAX/TSL EBSD system, equipped with a high-speed Digiview camera for pattern acquisition. The tensile tested specimens were prepared via standard metallographic grinding followed by polishing using silica gel. The specimens were then electropolished to obtain a sufficient Kikuchi pattern quality. A step size of 100 nm was first used to obtain an overview of the microstructure, then steps of 20 nm were used for subsequent high-resolution EBSD mapping. The TSL OIM software was used for data analysis.

A significant variation in the tensile properties was observed that depended on the initial grain size and distribution. Two conditions are discussed in more detail: namely, one with high yield strength (YS = 902 MPa; referred to as UFG-I) and low elongation to fracture (16%) and one with lower yield strength (YS = 711 MPa; referred to as UFG-II) and higher elongation (44%). It is worth noting that the more ductile UFG-II sample has a total elongation (44%) similar to that of a coarse-grained specimen (58%), though it has a much higher YS (703 MPa, i.e. three times that of the coarse-grained specimen, 210 MPa). The UFG-I sample was processed first by two thermal cycles at 950 °C, then by two ensuing cycles at 825 °C. For the UFG-II sample, the first and second cycles were conducted at 900 and 850 °C, respectively. Figure 1 shows the true stress–strain curves of the two specimens and their microstructures obtained via backscatter imaging. The grain size analysis conducted via the linear intercept method reveals that the sample UFG-I has about 60 area% of the grains in the size range of 200–500 nm. In contrast, sample UFG-II is characterized by a bimodal grain size distribution, with one group of crystals in the range 300–1000 nm and another in the range 1–2 μm. Apart from the YS and ductility, the strain hardening characteristics also depend on the respective grain size distributions: sample UFG-I exhibited poor strain-hardening ability, with a strain hardening exponent n of only 0.015. For this material, no strain softening was observed until the onset of necking. Sample UFG-II showed an exponent of 0.12, i.e. an order of magnitude higher than for UFG-I. The better strain-hardening potential of sample UFG-II yielded higher tensile strength and total elongation. As discussed below, we attribute this effect to the bimodal grain size distribution [10].

A detailed scanning electron microscopy and EBSD analysis of the post-tensile fractured specimens was conducted to better elucidate the underlying tensile deformation characteristics of the two specimens. The deformation microstructure analysis along the gauge length towards the fracture zone revealed major differences in deformation characteristics between the two samples, both within the necking region and close to the fracture zone. Sample UFG-I showed a very heterogeneous deformation microstructure, whereas sample UFG-II revealed more uniform deformation features. In sample UFG-II we observed very fine elongated grains that are uniformly spread across the entire specimen dimension. In contrast, sample UFG-I revealed three distinctly different regions: (i) fine grains (<500 nm), with little to no accumulated plastic deformation; (ii) rotation-induced grain coalescence; and (iii) shear bands. Figure 2 shows inverse pole figure maps consisting of both austenite and martensite phases of the area 1 mm away from the fracture tip for the two specimens. The tensile stress direction is in the horizontal direction of the inverse pole figure map.

Sample UFG-II exhibited nearly 62 area% of deformation-induced transformation of austenite to martensite. The elongated deformation-induced martensite (DIM) grains, represented by purple color coding in the inverse pole figure map, were of uniform size. The preferred crystal orientations of the DIM were close to the center of the inverse pole figure stereographic triangle. The larger DIM grains were characterized by a more pronounced change in orientation (red colors in Fig. 2, [0 0 1] texture). About 52 line% of the grain boundaries

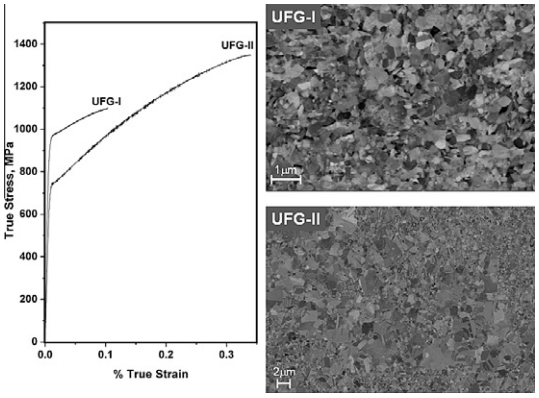

Figure 1. Tensile true stress–strain curves of UFG-I and II samples. The adjacent microstructures correspond to (i) UFG-I: ultrafine grains and (ii) UFG-II: bimodal grain size distribution.

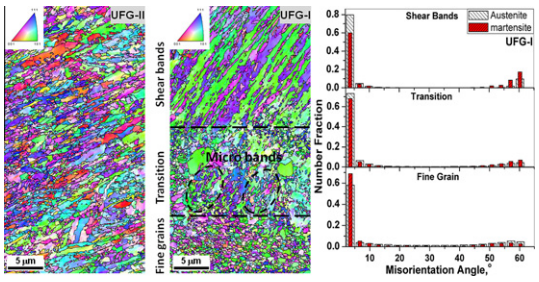

Figure 2. Inverse pole figure map of the UFG-I and UFG-II samples. The three regions: (i) fine grains, (ii) transition from fine grains to shear bands and (iii) shear bands, in sample UFG-I are marked. The presence of low-angle boundaries in the three regions of specimen UFG-I can be noted in the adjacent misorientation angle distribution plots. Austenite: green and cyan; martensite: purple, blue, orange and red. (For interpretation of the references to color in this figure legend, the reader is referred to the web version of this article.)

among the elongated DIM grains were characterized as low-angle grain boundaries. This observation indicates pronounced plastic deformation in these grains. The retained fine austenite grains, with initial orientations near the [0 1 1] direction parallel to the tensile axis, tend to rotate towards the center of [0 1 1]–[1 1 1] axis during deformation. The low-angle grain boundaries (75 line%) were found to be distributed within these grains as well as near the inherited high-angle grain boundaries.

The UFG-I sample, with low ductility, showed a transition stage of little or no deformed austenite grains to a massive shear banding zone (Fig. 2). This transition was assisted by deformation-induced grain rotation and coalescence. More specific orientation changes from the initial [0 1 1] position towards the center of the [0 1 1]–[1 1 1] axis were observed. These changes are indicated by the initial green to cyan color range in the inverse pole figure map. Only 31 area% deformation-induced transformation from austenite to DIM was found in the transition region. Both DIM and austenite grains showed a high density of low-angle grain boundaries (about 70 line%). These occurred mostly as intra-granular interfaces in DIM grains, whereas in the austenite grains they formed preferentially near high-angle grain boundaries and to a minor extent within the grains. A similar microstructure was observed in the adjacent fine undeformed austenite grain region. However, the arrangement of the low-angle grain boundaries of the austenite grains was mainly in the form of a grain boundary network. Also no substantial change in their initial orientation was found. The shear zone region showed extensive shape broadening of the bands and an increase in deformation-induced transformation of austenite (48 area% DIM), as represented by the purple color in the inverse pole figure map. The inter-phase boundaries were mainly high-angle grain boundaries. The low-angle grain boundary distribution in these bands was similar to that inside the fine undeformed region.

We observed the evolution of SBs in sample UGF-I near the fracture tip. This effect caused plastic instability, promoting early failure. We hence associate the small tensile ductility of this material with the formation of SBs. This contradicts previous studies [13,14], where plastic deformation in Fe and Fe–Cu alloys was considered to proceed via microshear banding and broadening. Wang et al. [15] observed SB formation in nc Cu via the rotation of fine grains [16] and their coalescence, leading to the formation of fine, elongated grains. This mechanism was claimed to support the formation of fine microbands, which at higher tensile stresses accommodate the flow stress by the formation and broadening of SBs. Also, Jia et al. [13] hypothesized that at sufficiently high stress levels small grains below 300 nm can reorient into orientations that offer soft shear modes. This triggers the associated geometrical softening, leading to shear localization [17]. The transition stage observed in this study appears to support the above hypothesis. The plastic deformation becomes localized within the reoriented grains in the SBs and the local work hardening results in spatial broadening of the SBs with increasing plastic strain. DIM formation, which is another way of consuming mechanical energy, is rare in the UFG austenite in the UFG-I sample because of the increase in the critical stress required for the deformation-induced transformation in fine grains [18]. This may have resulted in further loss of ductility. The observed increase in the DIM fraction inside the SBs can hence be understood in terms of the rotation-induced increase in the grain size inside the SB zones. On the other hand, the UFG-II sample attained higher tensile strength and ductility, mainly due to the enhanced DIM transformation of austenite. Analysis of the stress–strain curve (Fig. 1) did not reveal any inflection point which could be associated with the onset of DIM formation. We hence assume that continuous transformation from austenite to DIM occurs in specimen UFG-II [19]. To better elucidate this phenomenon, the volume fraction of DIM was determined along the gauge length towards the fractured end using a portable Feritscope MP 30E-S (Fisher, Germany). The Feritscope was calibrated with the reference standard NIST RM8480 and 8481 before the measurements. The true local strain was determined by measuring the change in the width at each DIM measurement location. The result is shown in Figure 3. This indicates continuous evolution of DIM in UFG-II, whereas in UFG-I it was high after necking to near the final fracture. Therefore, we suggest that the continuous evolution of DIM suppressed the formation of SBs and thus delayed necking [20]. In contrast, in the UFG-I material the retarded formation of DIM in the transition region enhanced the propensity for SB formation, causing early plastic instability and fracture.

The results show the deformation behavior of a standard austenitic stainless steel rendered to an UFG material by subjecting it to rapid thermal cycling. We observed that such steels with grain sizes below 500 nm undergo a transition in the deformation behav-

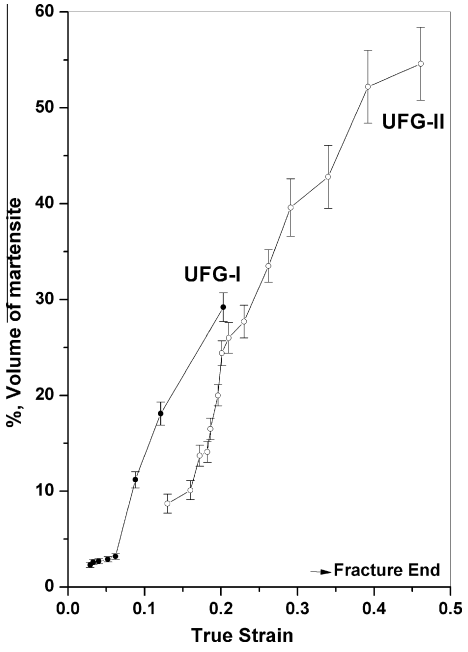

Figure 3. Change in the deformation-induced martensite volume per cent along the gauge length towards the fracture tip.

ior. This transition proceeds from initial dislocation-mediated grain-scale plastic deformation to strain localization at higher stresses, leading to shear banding, which finally cause premature failure and hence a loss in ductility. An alternative sample, UFG-II, with a bimodal grain size distribution, showed a much higher ductility and tensile strength. We interpret this behavior by a continuous deformation-induced transformation of austenite to martensite.

[1] R. Song, D. Ponge, D. Raabe, J.G. Speer, D.K. Matlock, Mater. Sci. Eng. A 441 (2006) 1.
[2] R. Song, D. Ponge, D. Raabe, Acta Mater. 53 (2005) 4881.
[3] D. Jia, Y.M. Wang, K.T. Ramesh, E. Ma, Y.T. Zhu, R.Z. Valiev, Appl. Phys. Lett. 79 (2001) 611.
[4] Y.M. Wang, M.W. Chen, F. Zhou, E. Ma, Nature (London) 419 (2002) 912.
[5] D. Farkas, H. Van Swygenhoven, P.M. Derlet, Phy. Rev. B 66 (2002) 060101.
[6] Y.M. Wang, K. Wang, D. Pan, K. Lu, K.J. Hemker, E. Ma, Scripta Mater. 48 (2003) 1581.
[7] K.S. Kumar, S. Suresh, M.F. Chisholm, J.A. Hortin, P. Wang, Acta Mater. 51 (2003) 387.
[8] Q.M. Wei, D. Jia, K.T. Ramesh, E. Ma, Appl. Phys. Lett. 81 (2002) 1240.
[9] Y.M. Wang, E. Ma, Mater. Sci. Eng. A 375–377 (2004) 46.
[10] Y.M. Wang, E. Ma, Acta Mater. 52 (2004) 1699.
[11] E. Ma, J. Metal 58 (2006) 49.
[12] B. Ravi Kumar, B. Mahato, Sailaja Sharma, J.K. Sahu, Metall. Mater. Trans. A 40 (2009) 3226.
[13] D. Jia, K.T. Ramesh, E. Ma, Acta Mater. 51 (2003) 3495.
[14] J.E. Carsley, A. Fisher, W.W. Milligan, S.A. Hackney, E.C. Aifantis, Metall. Mater. Trans. A 29 (1998) 2261.
[15] Y.M. Wang, E. Ma, M.W. Chen, Appl. Phys. Lett. 80 (2002) 2395.
[16] M. Upamanyu, D.J. Srolovitz, A.E. Lobkovsky, J.A. Warren, W.C. Carter, Acta Mater. 54 (2006) 1707.
[17] Q. Wei, D. Jia, K.T. Ramesh, E. Ma, Appl. Phys. Lett. 81 (2002) 1240.
[18] C.-S. Yoo, Y.-M. Park, Y.-S. Jung, Y.-K. Lee, Scripta Mater. 59 (2008) 7.
[19] J.E. Jin, Y.S. Jung, Y.K. Lee, Mater. Sci. Eng. A 449–451 (2006) 786.
[20] I. Sabirov, Y. Estrin, M.R. Barnett, I. Timokhina, P.D. Hodgson, Acta Mater. 56 (2008) 2223.